International Journal of Heat and Fluid Flow 104 (2023) 109229

Contents lists available at ScienceDirect

International Journal of Heat and Fluid Flow

journal homepage: www.elsevier.com/locate/ijhff

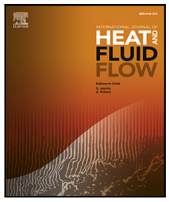

Direct numerical simulations and spectral proper orthogonal decomposition analysis of shocklet-containing turbulent channel counter-flows

Arash Hamzehloo [a,*,1], David J. Lusher [b,1], Neil D. Sandham [b,1]

[a] Turbulence Simulation Group, Department of Aeronautics, Imperial College London, London SW7 2AZ, United Kingdom
[b] Aerodynamics and Flight Mechanics Group, University of Southampton, Southampton SO16 7QF, United Kingdom

ARTICLE INFO

Keywords:
Counter-flow
Compressible turbulence
Shocklet
Direct numerical simulation
SPOD
Modal analysis
OpenSBLI

ABSTRACT

Counter-flow configurations in a confined channel flow provide an efficient framework to study high intensity turbulent mixing processes. In a previous study (Physical Review Fluids, 6(9), p.094603), a wall-bounded counter-flow turbulent channel configuration was presented as an effective framework for addressing certain challenges related to the study of compressibility effects on turbulence as an alternative to free shear layer and Poiseuille/Couette type flows. Here, the previous direct numerical simulations are extended to a higher Mach number ($M = 0.7$) to quantify direct and indirect effects of compressibility. It is found that the configuration is able to produce large numbers of embedded shocklets, leading to significant asymmetry in probability density functions of dilatation. Reducing the Prandtl number from 0.7 to 0.2 increases the compressibility effect further by reducing the bulk heating in the channel. A peak turbulent Mach number close to unity is obtained, for which the contribution of the dilatational dissipation to the total dissipation is nevertheless found to be limited to $\sim 6\%$. Indirect effects of compressibility are much larger, with changes of up to 40% in Favre normal stresses, despite the mean flow and shear stress being almost unaffected by compressibility in this configuration. Given the inflectional nature of the turbulent mean flow it is also interesting to identify large structures. Spectral Proper Orthogonal Decomposition (SPOD) reveals a full spectrum with a slow decay of energy with mode number. Mode shapes are three-dimensional with the low frequencies displaying elongated streaks in the velocity field at the channel centre plane.

1. Introduction

The effects of compressibility on the turbulent characteristics of fluid flows can be complex and significant. Such effects are typically manifested through, among others, reduction in turbulence production, acoustic/entropy oscillations, shear layer growth suppression, shock formation and non-linear shock-turbulence interactions (Lee et al., 1991; Lele, 1994; Sarkar, 1995; Freund et al., 2000). Many aspects of the complex interactions between compressibility effects and turbulence structures are still not thoroughly understood. Recent studies of shocklets include (Terakado et al., 2022), in which it was shown that such flow discontinuities were present for turbulent Mach numbers of $M_t \geq 0.7$. These shocklets were shown to modify sound generation mechanisms and vortex dynamics. Traditionally, free shear layers (such as jets, wakes and mixing layers) and Poiseuille/Couette type flows (such as channel flows) have been utilised to study compressible turbulence (Freund et al., 2000). Spatially-developing mixing layer simulations are computationally expensive and sensitive to far-field and inflow/outflow boundary conditions (Mankbadi et al., 2017; Yao and Hussain, 2020). However, basic compressibility effects can be captured in temporal simulations, as discussed by Vreman et al. (1996). One drawback of the temporal approach is that the shear layer thickens continually over time and computational grids suitable for later times are inefficient during the early development stages of the flow. On the other hand, Poiseuille/Couette type flows are relatively computationally efficient (Kim et al., 1987; Coleman et al., 1995; Johnstone et al., 2010) and can achieve high Reynolds numbers at a much lower cost compared to what is typically required for spatially-developing boundary layers (Coleman et al., 1995). However, conventional channel flows have limitations in terms of the achievable fluctuating Mach number due to the increase in the mean flow temperature and the associated speed of sound, without the use of artificial heat sinks. A counter-flow configuration can potentially overcome the barriers of the above-mentioned flows.

Counter-flows are recognised as highly efficient configurations for mixing, thanks to the maintenance of high turbulence intensities (Humphrey and Li, 1981; Strykowski and Wilcoxon, 1993; Forliti et al.,

* Corresponding author.
E-mail address: a.hamzehloo@imperial.ac.uk (A. Hamzehloo).
[1] All authors have contributed equally.

https://doi.org/10.1016/j.ijheatfluidflow.2023.109229
Received 27 March 2023; Received in revised form 18 September 2023; Accepted 4 October 2023
Available online 11 October 2023

Nomenclature

a_c	Local speed of sound
$\Delta x^+, \Delta y^+, \Delta z^+$	Normalised cell sizes in different directions
δ_{ij}	Kronecker delta
ϵ^D	Dilatational viscous dissipation
ϵ^S	Solenoidal viscous dissipation
ϵ^T	Total viscous dissipation
γ	Ratio of specific heats
$\langle\rangle$	Averages over the homogeneous spatial directions and time
$\langle\rangle_b$	Additional bulk average over y
$\langle M\rangle$	Mean Mach number
μ	Dynamic viscosity
ϕ	An arbitrary flow quantity
ϕ''	Turbulent fluctuation of an arbitrary with respect to the Favre average
ϕ'	Turbulent fluctuation of an arbitrary flow quantity
ρ	Density
τ_t	Time scale
τ_{ij}	Viscous stress tensor
θ	Dilatation
$\tilde{y}$	Coordinate in the y direction relative to the wall
$\tilde{y}^+$	Normalised wall distance
ζ	Dilatation value threshold
$\{\phi\}$	Favre average of an arbitrary flow quantity
$_b$	Subscript b denotes bulk average
$_p$	Subscript p denotes the peak value of a flow quantity
$_{wall}$	Subscript $wall$ denotes the value at the wall
a	Coefficient in the forcing term
c_0	Maximum amplitude of forcing term
c_j	Forcing term
E	Total energy
f	Frequency
H	Channel half height
M	Mach number set in the simulation
M_t	Turbulent Mach number
p	Pressure
Pr	Prandtl number
q_j	Heat flux
Re	Reynolds number set in the simulation
T	Temperature
t	Time
u	Velocity component in the x direction
u_i	Velocity component in the ith direction
$u_i''u_j''$	Reynolds stresses
u_τ	Friction velocity
u^*_{ref}	Reference velocity, with $*$ denoting a dimensional quantity here and elsewhere
v	Velocity component in the y direction
w	Velocity component in the z direction
x_j	Spatial coordinate in the jth direction ($j = 1, 2, 3$ correspond to x, y, z respectively)

2005). Moreover, they have been utilised in the development of flow control mechanisms, such as thrust vectoring applications (Strykowski et al., 1996; Alvi and Strykowski, 1999; Gillgrist et al., 2007), as well as low-emission combustors (Lonnes et al., 1998). The use of counter-flow configurations for fundamental flow studies was first recognised by Humphrey and Li (1981) and later by various researchers, including most notably Forliti et al. (2005) who concluded that locally unstable flows trigger a global instability in planar counter-flow shear layers. Previously, we introduced (Hamzehloo et al., 2021a) a wall-bounded counter-flow turbulent channel configuration, amenable to Direct Numerical Simulation (DNS), and demonstrated that it could overcome the barriers associated with free shear layers and Poiseuille/Couette type flows. Specifically, it retains a statistically stationary one-dimensional solution, in common with conventional channel flows, but contains an inflectional mean flow, representative of free shear layers. The counter-flow channel has periodic streamwise and spanwise boundaries and isothermal no-slip walls and is driven by a mean pressure gradient introduced by a hyperbolic tangent forcing term. The unstable base flow of the proposed counter-flow is more relevant to the free shear layers found in practical applications, such as jets, wakes, and mixing layers, compared to another version of channel flow that produces counter-flows of the kind considered here with a linearly stable base flow, as discussed by Waleffe (1990). It was previously shown (Hamzehloo et al., 2021a) that when the peak local mean Mach number reached $\sim$0.55, a turbulent Mach number of $\sim$0.6 could be obtained, indicating that such counter-flow configuration could potentially be useful for studying compressibility effects on turbulence.

The previous study (Hamzehloo et al., 2021a) provided insights into flow dynamics of the counter-flow configuration up to a Mach number of $M = 0.4$ (defined based on a reference velocity deduced from the forcing as discussed in the next section). However, this maximum Mach number was constrained by the necessity of a shock-capturing method for higher values and the associated increase in computational cost. To address this limitation, the primary objective in this study is to identify strong compressibility effects in counter-flow channels. We accomplish this by enhancing our numerical treatment in the vicinity of flow discontinuities with an efficient high-order characteristic-based shock-capturing approach (Yee and Sjögreen, 2018; Lusher et al., 2023), thereby extending the previous DNS investigation to a Mach number of $M = 0.7$. This extension allows us to capture the formation and evolution of shocklets, and their interactions with turbulence. A secondary objective is to deepen our understanding of the characteristics and interactions of these highly three-dimensional transient shocklets with the turbulent scales. To this end, we utilise Spectral Proper Orthogonal Decomposition (SPOD) (Schmidt and Towne, 2019), a data-driven technique designed to analyse the spatio-temporal characteristics of a flowfield, as a tool for modal analysis of the high-Mach counter-flow field.

The SPOD methodology provides a frequency-resolved modal decomposition (Towne et al., 2018; Muralidhar et al., 2019), enabling the extraction of fluid dynamical structures (Abdelsamie et al., 2017; Muralidhar et al., 2019; Abreu et al., 2020). Most of these applications have been to incompressible flows, but SPOD has also recently been applied to transonic aerofoil buffet flows where a global instability is active (Moise et al., 2022). The present flow is a new application for SPOD, in that it is an internal compressible turbulence problem. The temporal nature of the flow and the presence of an inflection point in the mean flow suggest that energy is fed into large-scale structures by the mean flow instability and it is of interest to check with SPOD the organisation of such structures and whether any particular frequencies/wavenumbers are preferred. SPOD decomposes the flowfield into orthogonal modes, each representing a distinct pattern of variation, ranked according to their significance in the frequency domain. The first mode captures the greatest variability, with subsequent modes progressively representing smaller amounts of variability (Schmidt and Towne, 2019; Schmidt, 2022).

The outline of this paper is as follows: in Section 2, the governing equations, numerical methods, computational framework and problem

Table 1
DNS counter-flow channel cases.

Case	M	Re	Pr	WENO filter	Δt	$\{u\}_b$	$\{u\}_p$	$\langle a_c\rangle_b$	$\langle a_c\rangle_p$	$\langle T\rangle_p$	$\langle M\rangle_p$	M_{t_p}
1	0.1	400	0.7	No	2×10^{-4}	1.409	2.159	10.291	10.479	1.098	0.207	0.213
2	0.4	400	0.7	No	5×10^{-5}	1.375	2.047	3.669	3.849	2.374	0.556	0.595
3	0.4	400	0.7	Yes	5×10^{-5}	1.380	2.062	3.671	3.852	2.376	0.560	0.594
4	0.7	400	0.7	Yes	5×10^{-5}	1.358	2.005	2.919	3.132	4.823	0.697	0.758
5	0.7	400	0.2	Yes	5×10^{-5}	1.535	2.238	2.382	2.602	3.332	0.973	0.981

setup are introduced. In Section 3, first the key mean flow and turbulence statistics are discussed. Then, the formation, structure and evolution of the transient shocklets in highly compressible counter-flows are studied and quantified in Section 3.2. Finally, SPOD analysis of a high-Mach counter-flow case is discussed in Section 3.4 . Further discussion and final conclusions are drawn in Section 4.

2. Methodology

2.1. Governing equations

The dimensionless governing equations of a compressible Newtonian fluid flow, that conserve mass, momentum and energy, are solved as (Hamzehloo et al., 2021a):

$$\begin{aligned}
&\frac{\partial \rho}{\partial t} + \frac{\partial}{\partial x_j}(\rho u_j) = 0,\\
&\frac{\partial \rho u_i}{\partial t} + \frac{\partial}{\partial x_j}(\rho u_i u_j + p\delta_{ij} - \tau_{ij}) + c_j\delta_{ij} = 0,\\
&\frac{\partial \rho E}{\partial t} + \frac{\partial}{\partial x_j}(\rho E u_j + u_j p + q_j - u_i\tau_{ij}) + c_j u_j = 0,
\end{aligned} \tag{1}$$

where ρ represents the density, $u_i (i = 1,2,3)$ denotes the velocity component (u, v and w, respectively) in the ith direction (x, y and z, respectively), E is the total energy, and p and δ denote the pressure and the Kronecker delta, respectively. The forcing term c_j drives the flow. In the x direction, its value is given by $c_1 = -c_0 \tanh(ay)$, while it is zero in all other directions. The amplitude of the forcing term is set as $c_0 = 1$. The bulk-averaged density $\langle \rho^* \rangle_b$ is used as a reference, where * denotes a dimensional quantity and angle brackets denote averages over the homogeneous spatial directions (x and z) and time t. The characteristic length is the channel half height H^*. The reference velocity is deduced from the forcing as $u^*_{\text{ref}} = \sqrt{c_0^* H^* / \langle \rho^* \rangle_b}$. A reference timescale is defined by H^*/u^*_{ref}, which is subsequently used to form the dimensionless frequency f.

The viscous stress tensor (τ_{ij}) and the heat flux (q_j) are defined as:

$$\tau_{ij} = \frac{\mu}{Re}\left(\frac{\partial u_i}{\partial x_j} + \frac{\partial u_j}{\partial x_i} - \frac{2}{3}\frac{\partial u_k}{\partial x_k}\delta_{ij}\right), \tag{2}$$

$$q_j = \frac{-\mu}{(\gamma-1)M^2 Pr Re}\frac{\partial T}{\partial x_j}, \tag{3}$$

where μ denotes the dynamic viscosity, T is the temperature, γ is the ratio of specific heats with a value of $\gamma = 1.4$ here and Pr is the Prandtl number. Re and M denote the Reynolds and Mach numbers set in the simulation, based on the reference velocity together with the channel half height and the wall temperature and viscosity. The temperature-dependent dynamic viscosity is calculated via a power law as $\mu = T^{0.7}$.

Equivalent driving forces are applied in opposite directions to the upper ($y > 0$) and lower ($y < 0$) halves of the domain ($-1 \leq y \leq 1$), which consequently result in the formation of a shear-forcing or counter-flow condition. The coefficient a in the hyperbolic tangent forcing term is positive with a value of $a = 100$. The total energy E, is related to the pressure p and temperature T of the perfect gas as $p = (\gamma-1)(\rho E - \rho u_i u_i/2) = \rho T/(\gamma M^2)$. where the temperature is normalised with the wall temperature.

A 4th-order non-dissipative finite-difference central scheme is used to discretise the governing equations and grid metrics. Convective terms are recast in a quadratic split formulation (Feiereisen, 1981) to improve numerical stability and reduce aliasing errors. A 4th-order one-sided boundary scheme (Carpenter et al., 1999) is used at non-periodic boundaries to maintain consistent spatial discretisation order throughout the domain. Viscous terms are solved in Laplacian form by dedicated second-derivative operators to avoid odd-even decoupling phenomena (Pirozzoli, 2011). A 5th-order Global Lax–Friedrichs (GLF) Weighted Essentially Non-Oscillatory (WENO) filter-step method (Yee and Sjögreen, 2018) is applied to the flowfield after the completion of each full time-step to stabilise the simulation in the presence of shocklets. The density field is corrected if necessary, after applying the filtering to maintain the conservation of mass. A low-storage three-stage explicit 3rd order Runge–Kutta scheme (Williamson, 1980) is used to advance the solution in time. The time-steps, as outlined in Table 1, were determined empirically, but can be compared with predictions based on combined convective and viscous Courant–Friedrichs–Lewy (CFL) conditions, as discussed by Li (2003). For example, in the counter-flow case with the strongest compressibility effects ($M = 0.7$ and $Pr = 0.2$), the time-step employed was required to be approximately 7.5 times smaller than the predicted analytical time-step. This indicates that this CFL estimate is not accurate for highly compressible turbulence. Additionally, boundary condition implementations, grid metrics, shock sensors, and differences in the stability characteristics of numerical scheme formulations can all contribute to variations seen in time-step requirements (Pirozzoli, 2011; Brehm et al., 2015). The work of Modesti and Pirozzoli (2016) reported a factor of two difference in permissible time-step for compressible turbulent channel flows depending on whether or not staggered grid locations were used for placement of the walls.

All of the simulations presented in this work were computed in OpenSBLI 2.0, a Python-based automatic source code generation and parallel computing framework for compressible fluid dynamics on structured meshes (Lusher et al., 2021). OpenSBLI utilises symbolic algebra to automatically generate C/C++ codes for the Oxford Parallel library for Structured mesh solver (OPS), an embedded domain specific language with associated libraries and pre-processors to generate parallel executables for applications on multi-block structured meshes (Reguly et al., 2014; Mudalige et al., 2019). In the context of the present work, OpenSBLI has been validated for simulations of compressible wall-bounded turbulence by Hamzehloo et al. (2021b) and Lusher and Coleman (2022). The results presented here are obtained using multiple NVIDIA P100 and A100 GPUs using CUDA+MPI.

2.2. Problem specifications

As shown schematically in Fig. 1, the streamwise and spanwise boundaries of the counter-flow channel configuration are periodic, while isothermal ($T_w = 1.0$) no-slip viscous wall conditions are enforced on the boundaries in the normal direction (y). In order to accurately resolve the near wall region, the grid is stretched symmetrically in the y direction (Hamzehloo et al., 2021b). We have previously identified an optimum domain size of $12H \times 2H \times 6H$ with a grid resolution of $240 \times 151 \times 200$ (Hamzehloo et al., 2021a). This domain size is used with a Reynolds number of $Re = 400$. Mach number values of $M = 0.1, 0.4$ and 0.7 are examined. The Prandtl number has a value of mainly $Pr = 0.7$. However, a case with $Pr = 0.2$ ($M = 0.7$) is also studied. This reduction in Prandtl number increases the heat flux

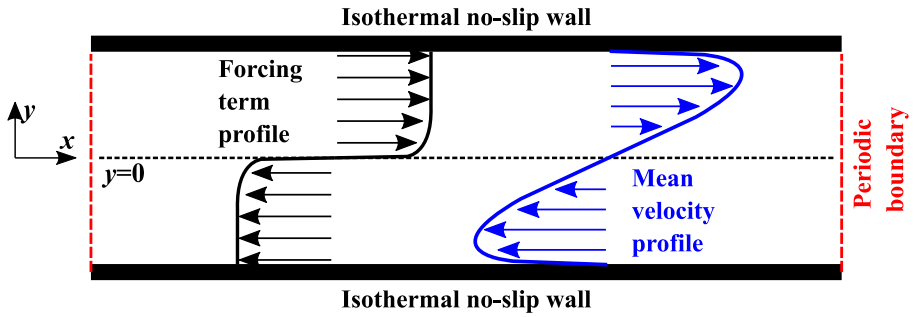

Fig. 1. 2D schematic of the 3D counter-flow channel configuration. The spanwise z direction into the page is also periodic.

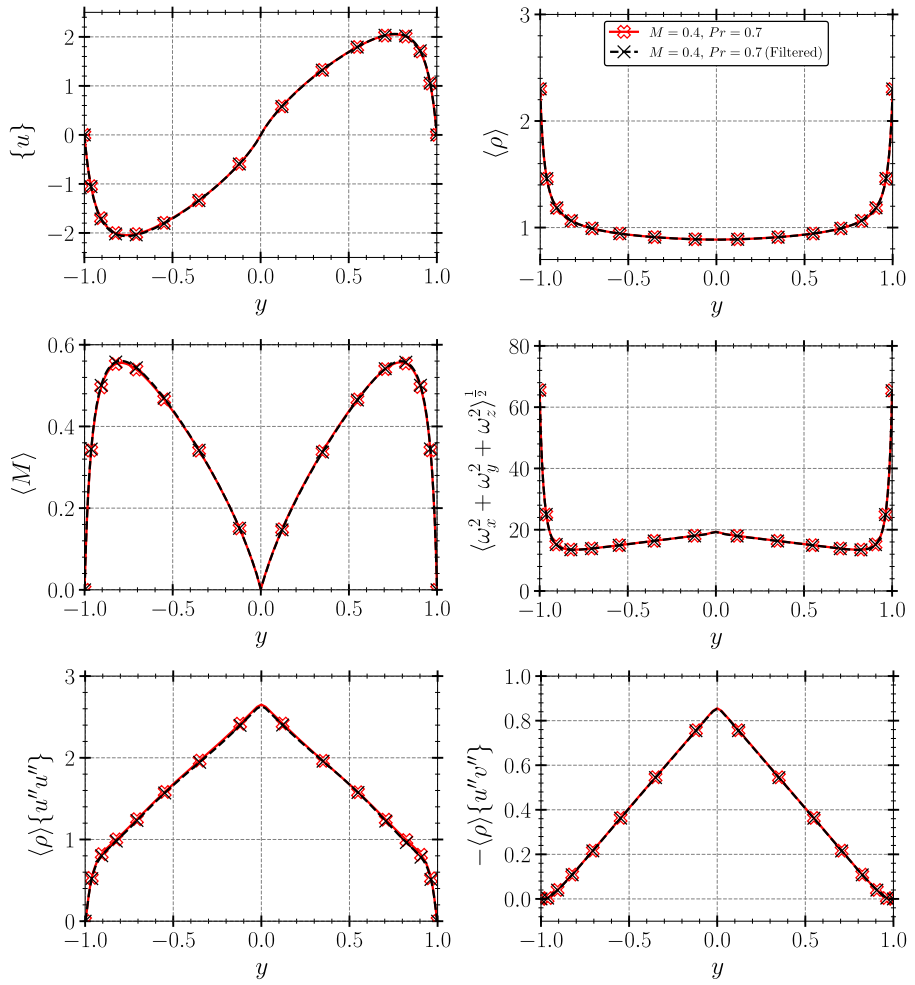

Fig. 2. Profiles of the mean velocity, density, Mach number, and vorticity fluctuation, and Favre streamwise normal and shear stresses for the counter-flow cases with $M = 0.4$ and with and without the WENO filtering.

through the isothermal walls, reducing the bulk temperature and sound speed in the channel, leading to increased local Mach numbers and stronger compressibility effects. The WENO filtering described in Section 2.1 is necessary to obtain a stable solution for the more numerically challenging cases at $M = 0.7$. For the case with $M = 0.4$, results of two simulations with and without the filtering are provided to make direct comparisons and examine the filtering effect. A list of test cases studied here is presented in Table 1. The key computational parameters and normalised grid resolutions based on the friction velocity (u_τ) is provided in Table 2. It should be noted that, here, subscript p denotes the peak values of flow quantities. The normalised wall distance value ($\tilde{y}^+$) is defined as $\tilde{y}^+ = \tilde{y}Re_\tau$, where $\tilde{y}$ is the coordinate in the y direction relative to the wall. The normalised cell sizes in different directions, Δx^+, $\Delta\tilde{y}^+$ (the height of the first grid point above the wall) and Δz^+, are evaluated in a similar way to $\tilde{y}^+$. The friction Reynolds number is defined as $Re_\tau = \langle\rho_{wall}\rangle u_\tau H/\langle\mu_{wall}\rangle$ where $u_\tau = \sqrt{\langle\tau_{wall}\rangle/\langle\rho_{wall}\rangle}$.

In this paper, the single prime ($'$) denotes the turbulent fluctuation which for an arbitrary flow quantity (ϕ) is defined as $\phi' = \phi - \langle\phi\rangle$. Moreover, for the higher Mach number case, the Favre average is defined as $\{\phi\} = \langle\rho\phi\rangle/\langle\rho\rangle$ and the double prime ($''$) denotes the turbulent fluctuation with respect to the Favre average defined as $\phi'' = \phi - \{\phi\}$. For the Reynolds stresses, the Favre average is related to the Reynolds average as $\langle\rho\rangle\{u_i''u_j''\} = \langle\rho u_i u_j\rangle - \langle\rho\rangle\langle u_i\rangle\langle u_j\rangle$. Also, the mean Mach number is defined as $\langle M\rangle = \sqrt{\langle u\rangle^2 + \langle v\rangle^2 + \langle w\rangle^2}/\langle a_c\rangle$, where a_c is the local speed of sound, while the turbulent Mach number is defined as $M_t = \sqrt{\langle u'u'\rangle + \langle v'v'\rangle + \langle w'w'\rangle}/\langle a_c\rangle$.

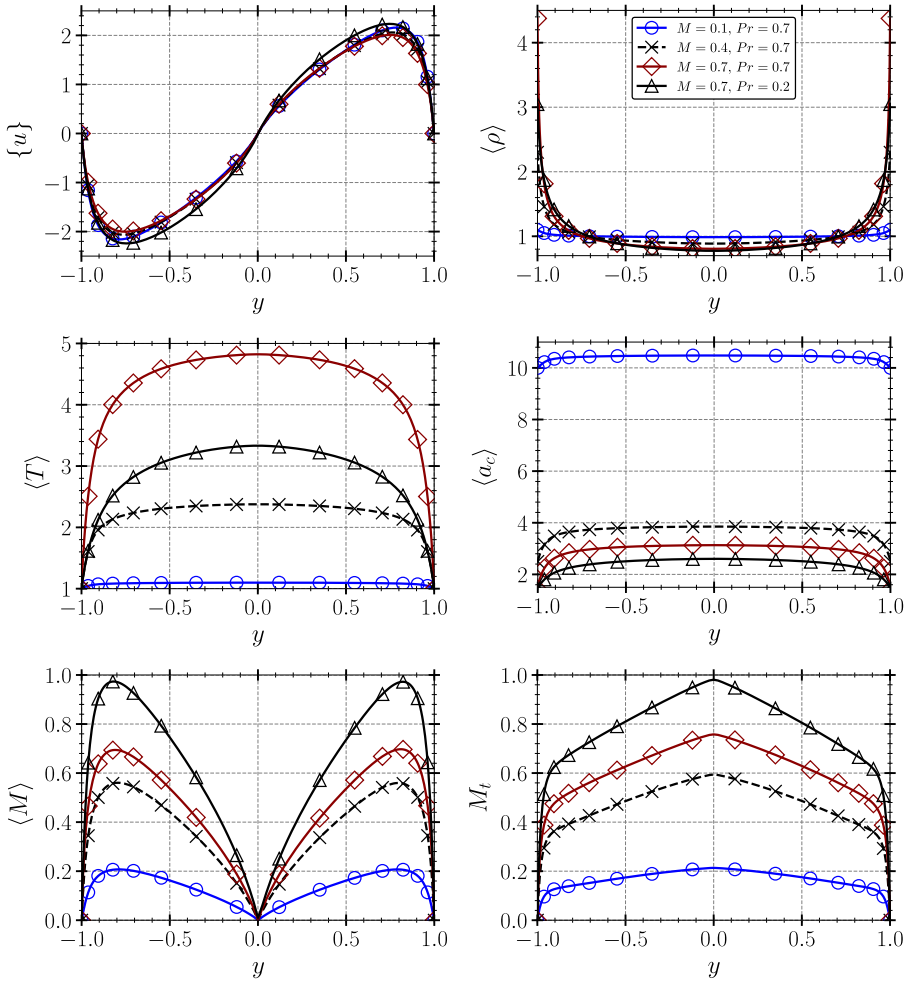

Fig. 3. Profiles of the mean velocity, density, temperature, speed of sound and Mach number, and profile of the turbulent Mach number (M_t).

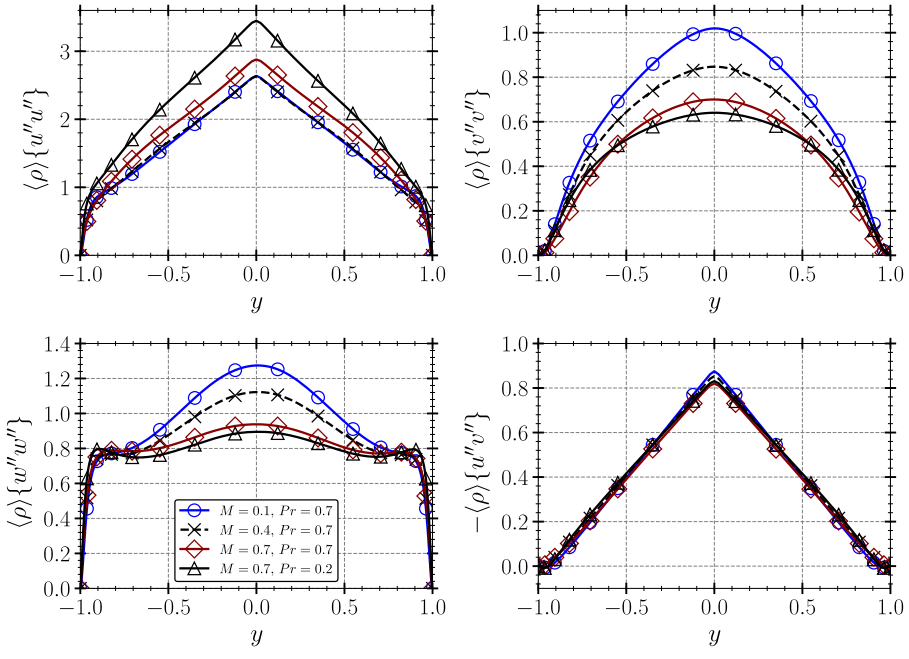

Fig. 4. Profiles of the Favre Reynolds stresses.

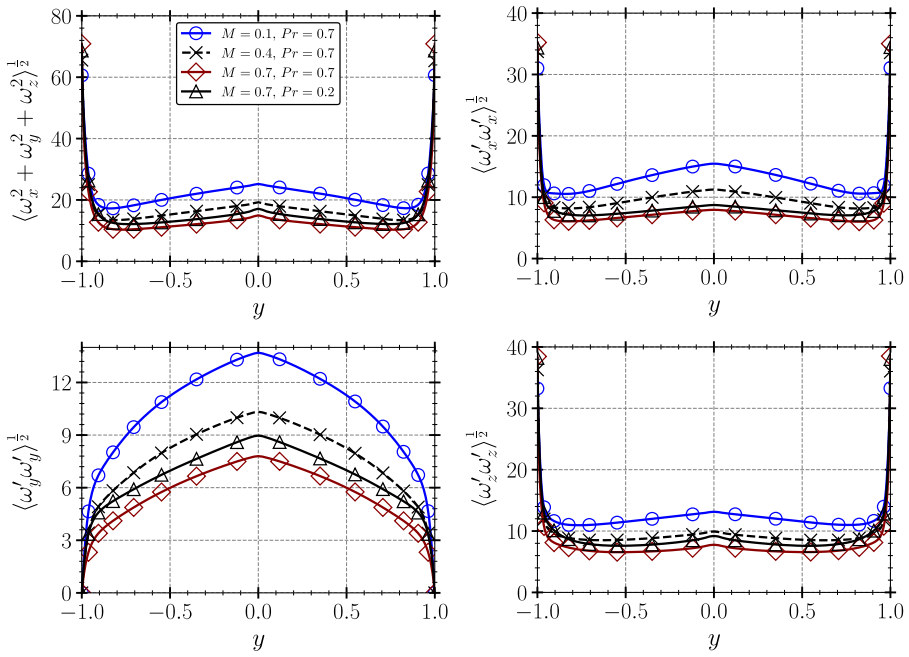

Fig. 5. Profiles of the vorticity fluctuation and the components of the vorticity turbulent fluctuations.

Table 2
Computational parameters of the counter-flow cases.

Case	M	Pr	WENO filter	Re_τ	u_τ	Δx^+	$\Delta \tilde{y}^+$	Δz^+	$\langle u \rangle_p^+$
1	0.1	0.7	No	131.482	0.299	6.574	0.406	3.944	7.209
2	0.4	0.7	No	193.835	0.210	9.691	0.599	5.815	9.716
3	0.4	0.7	Yes	194.769	0.211	9.738	0.602	5.843	9.742
4	0.7	0.7	Yes	278.672	0.159	13.933	0.862	8.360	12.631
5	0.7	0.2	Yes	231.122	0.189	11.556	0.715	6.933	11.790

2.3. WENO filtering

As introduced in Section 2.1, the code used by Hamzehloo et al. (2021a) is extended in the present work to include a filtering method based on the widely used family of WENO shock-capturing schemes. The filter is used to damp oscillations in the solution (due to sharp gradients from non-linear shocklets), while preserving the ability to resolve small-scale turbulence (Yee and Sjögreen, 2018). The WENO procedure works by constructing a high-order polynomial approximation of the solution is using a selection of smaller candidate stencils over neighbouring grid points (Jiang and Shu, 1996; Shu, 1997). The specific polynomial degree and stencil size depend on the order of the WENO method. In the present work, a 5th-order WENO scheme is applied. The weights for each lower-order approximation candidate stencil are calculated based on their ability to minimise the smoothness indicator, which is a measure of the smoothness of the solution in the stencil. The final reconstruction is built from a weighted combination of the smaller candidate stencils. The WENO reconstruction procedure is performed in characteristic space to enhance the robustness of the shock-capturing.

As in the framework presented by Yee and Sjögreen (2018), the WENO filtering is applied only once at the end of every time-step, rather than at every sub-stage of the Runge-Kutta time-stepping algorithm. The filter method subtracts a centred approximation to the WENO flux to leave only the dissipative portion of the WENO scheme. This dissipative contribution is then used to filter each of the conservative variables to selectively remove high-frequency oscillations in the solution while preserving the key turbulent structures. A modified version (Lusher and Sandham, 2019) of the Ducros sensor (Ducros et al., 2000) is used to localise the application of the shock-capturing only to regions containing shocklets. The WENO filter step method was validated in OpenSBLI for a supersonic Taylor–Green vortex case at $M = 1.25$ by Lusher et al. (2023), and was shown to have excellent numerical resolution while still remaining stable in the presence of strong shocks.

The counter-flow with $M = 0.4$ forms a mildly compressible turbulent flow with $M_{tp} \approx 0.6$ (Hamzehloo et al., 2021a), hence the formation of flow discontinuities in form of shocklets would be extremely limited. Therefore, the WENO filtering, which is only active where a discontinuity exists, should have a very limited role for the counter-flow with $M = 0.4$. Fig. 2 shows a direct comparison between various flow quantities (which will be discussed later in this paper) for the $M = 0.4$ counter-flow case with and without the WENO filtering. It is clear that these cases exhibit almost identical trends and Table 1 shows less than ~1% changes in their key flow quantities. This suggests that the filter-based shock capturing method is performing well and the grid resolution is fine enough. In the rest of this work, all results shown for $M \geq 0.4$ are obtained using the aforementioned WENO filtering scheme.

2.4. Spectral Proper Orthogonal Decomposition (SPOD)

SPOD, an extension of the Proper Orthogonal Decomposition (POD) method, can be used to identify the most important spatio-temporal modes of a dataset (Towne et al., 2018). To perform such an analysis, the data is first transformed into the frequency domain using Fourier transforms with overlapping segments. Then POD is applied to the frequency-domain data to identify the significant modes (those with larger eigenvalues). This allows for the identification of the dominant spatial patterns in the data for specific frequencies. The SPOD modes are temporally orthogonal and monochromatic, and are less noisy compared to Fourier analysis alone. In the present study, the memory-efficient streaming SPOD algorithm and software provided by Schmidt and Towne (2019) and Schmidt (2022) are used. Both $x - y$ (at $z = 0$)

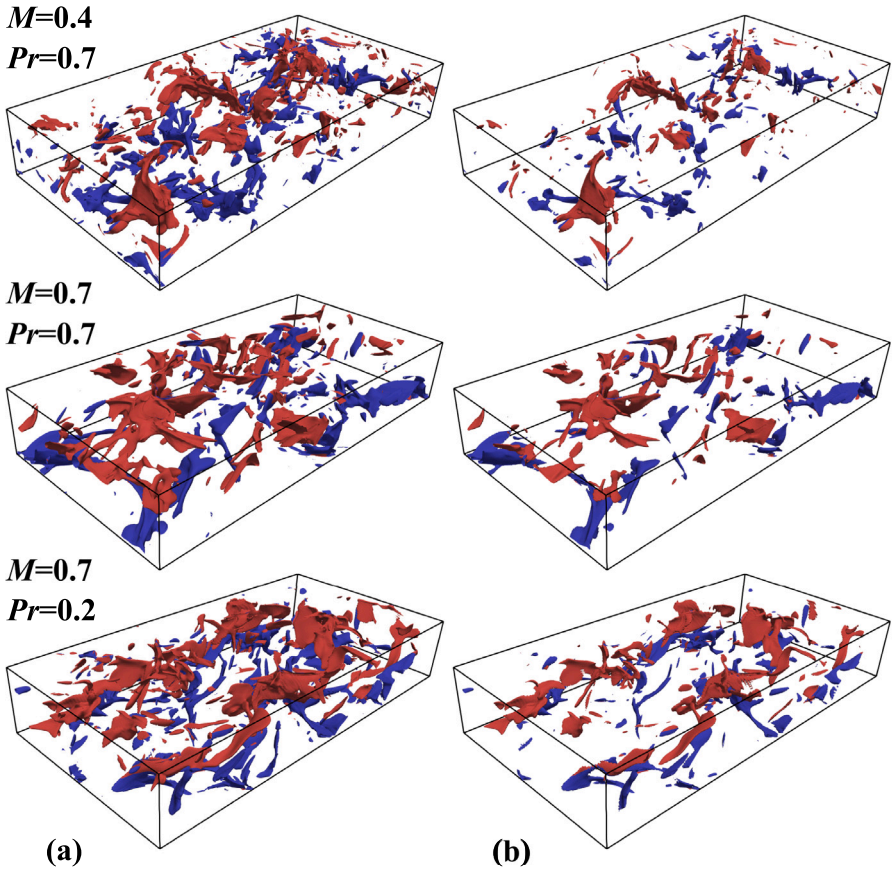

Fig. 6. Iso-surfaces of the dilatation with iso-values of (a): $\theta_{iso} = 2\theta'_b$ and (b): $\theta_{iso} = 3\theta'_b$. Red and blue colours show the flow directions in the positive (left to right) and negative streamwise directions, respectively.

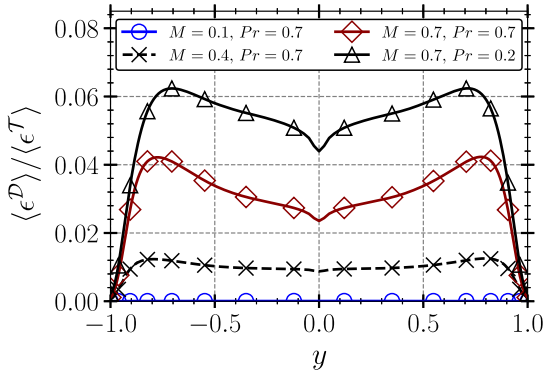

Fig. 7. Profiles of the ratio of the dilatational dissipation over the total dissipation.

and $x-z$ (at $y = 0$) planes of the counter-flow with $M = 0.7$ and $Pr = 0.7$ are investigated for both the u and v components of the velocity vector. Snapshots are stored at every 20 time-steps (i.e. $t = 0.001$) which results in a total of 330 000 samples. These are divided into segments, or blocks, which are concatenated into a matrix for the main analysis. The size and overlap of the blocks can be altered to balance the trade-off between frequency resolution and statistical accuracy (Schmidt and Towne, 2019). Here, a block number of 7 with 50% overlap and a Hamming window (to improve the accuracy by reducing the effects of spectral leakage (Schmidt, 2022)) have been selected. The SPOD formulation is omitted here for the sake of brevity, and the reader is to referred to the work by Moise et al. (2022) which applied the same methodology to compressible airfoil flows.

3. Results and discussion

3.1. Mean flow and turbulence statistics

Fig. 3 shows a direct comparison between the counter-flows studied here based on various mean flow quantities, including the streamwise velocity $\{u\}$, density $\langle\rho\rangle$, temperature $\langle T\rangle$, local speed of sound $\langle a_c\rangle$ and Mach number $\langle M\rangle$, and also the turbulent Mach number M_t. Additionally, Fig. 4 provides the Favre Reynolds stresses of the counter-flows. The temperature field is observed to have a strong dependence on the reference Mach number. For cases with increasing Mach number, for instance, as also provided in Table 1, the peak mean temperature is ∼2.0 and ∼4.4 times higher for the cases with $M = 0.4$ and $M = 0.7$ compared to the case at $M = 0.1$, respectively. Meanwhile, reducing the Prandtl number from $Pr = 0.7$ to 0.2 for $M = 0.7$ increases the thermal diffusivity in the simulation, and leads to a subsequent reduction in the peak mean temperature by ∼31%. As shown in Fig. 3, the mean velocity profiles do not change significantly when altering the Mach number since the latter is governed primarily by the local speed of sound. Mean and turbulent Mach numbers exhibit significant surges as the reference Mach number increases. Notably in the context of eddy-shocklet generation discussed later in this work, the peak turbulent Mach number increases by ∼179% and ∼256% when the reference Mach number is increased from $M = 0.1$ to $M = 0.4$ and 0.7, respectively. Reducing the Prandtl number while keeping the Mach number fixed at $M = 0.7$ further increases the turbulent Mach number by ∼29.5% to reach a value of near unity at the centreline of the channel. At these highly compressible flow conditions, strong non-linearities can develop within the flow (Lee et al., 1991; Samtaney et al., 2001).

Regarding the normal stresses, as shown in Fig. 4 and Table 3 (which presents the variation of the peak values of the Favre Reynolds

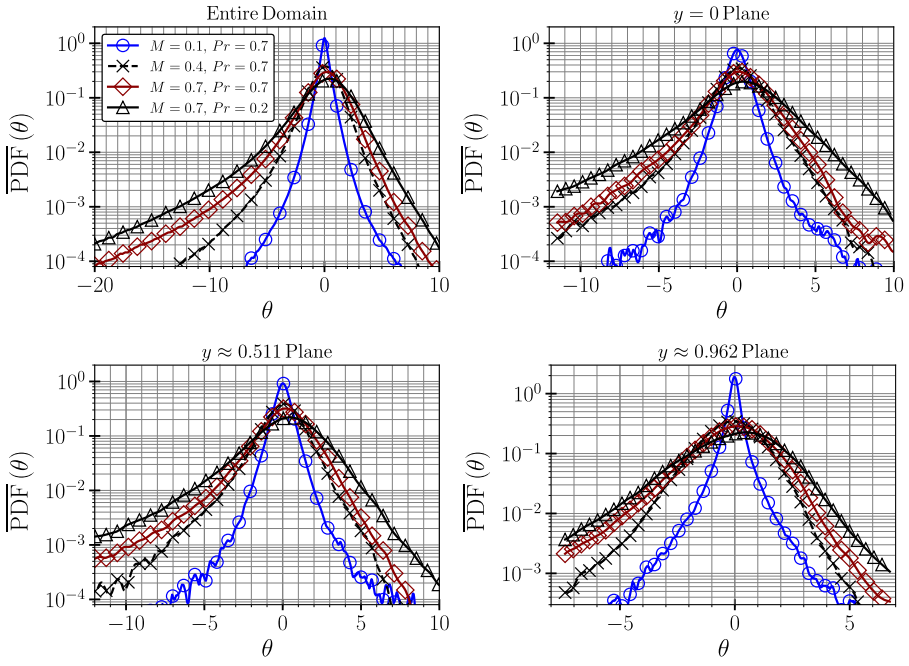

Fig. 8. Probability distribution of the dilatation over the entire domain and also specific $x - z$ planes (average over four independent realisations).

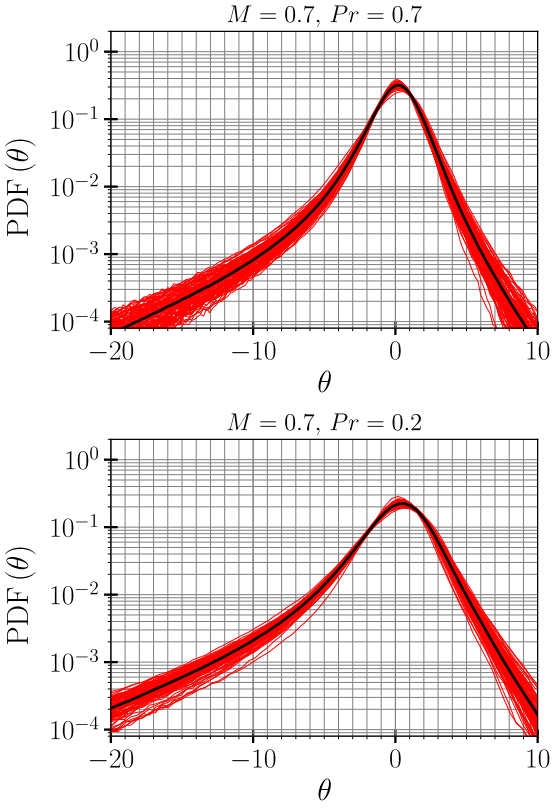

Fig. 9. Probability distributions of the dilatation over the entire domain for every $t = 10$ intervals up to $t = 1000$.

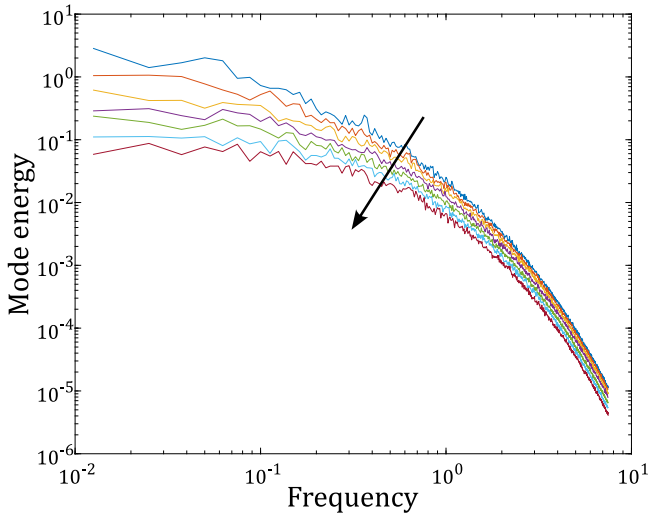

Fig. 10. Energy of the SPOD modes versus frequency. The black arrow illustrates the direction that the mode number increases ($M = 0.7$ and $Pr = 0.7$).

Table 3
Peak values of the Favre Reynolds stresses.

Case	M	Pr	$\langle\rho\rangle\{u''u''\}_p$	$\langle\rho\rangle\{v''v''\}_p$	$\langle\rho\rangle\{w''w''\}_p$	$-\langle\rho\rangle\{u''v''\}_p$
1	0.1	0.7	2.638	1.019	1.274	0.875
3	0.4	0.7	2.631	0.847	1.122	0.853
4	0.7	0.7	2.879	0.699	0.938	0.819
5	0.7	0.2	3.447	0.640	0.895	0.831

stresses with changes in the Mach and Prandtl numbers) a clear trend can be observed as the Mach number increases (cases 1,3 and 4), keeping Pr constant. For instance, when comparing Case 1 ($M = 0.1, Pr = 0.7$) with Case 4 ($M = 0.7, Pr = 0.7$), it can be observed that $\langle\rho\rangle\{u''u''\}_p$ increases by approximately 9%, from 2.638 to 2.879. Similarly, $\langle\rho\rangle\{v''v''\}_p$ and $\langle\rho\rangle\{w''w''\}_p$ decrease by ~31% and ~26% respectively. Thus, there is a clear linkage between changes in the Mach number and the state of turbulence anisotropy. The increase in anisotropy suggests a propensity towards a more one-dimensional or longitudinal turbulence state, while momentum transfer by the v and w velocity components is reduced. The changes in the streamwise fluctuation of $\langle\rho\rangle\{u''u''\}_p$ seen in Fig. 4 are notably smaller than in the other components, with no changes as M increases from 0.1 to

Table 4
Bulk-averaged dilatation fluctuation dependence on the reference Mach and Prandtl numbers.

Case	M	Pr	θ'_b
1	0.1	0.7	0.128
3	0.4	0.7	1.374
4	0.7	0.7	1.885
5	0.7	0.2	2.808

0.4 and then a small increase from 0.4 to 0.7. The effect of reducing Pr is consistent with the trend of increasing anisotropy with increases in the turbulence Mach number. There are some subtle differences however. The decrease in Pr affects $\langle\rho\rangle\{u''u''\}_p$ more than the transverse component, suggesting that the change in the bulk temperature also has a role to play. In summary, we can say that anisotropy of the turbulence increases with increasing M_t. With increasing M while keeping Pr constant, this mainly occurs by reductions in the transverse components of the Favre stresses, while for constant M and reducing Pr this happens mainly by increasing the streamwise Favre stress.

The overall vorticity fluctuation, $\omega' = \sqrt{\langle\omega_x^2 + \omega_y^2 + \omega_z^2\rangle}$ and the contributing components of the vorticity fluctuations are shown in Fig. 5. Trends in vorticity fluctuations for varying Mach and Prandtl numbers can be considered indicative of changes in the behaviour of smaller scales of turbulence, relative to the Favre stresses discussed in the previous paragraph. From Fig. 5, we can see that vorticity (the total and all the components individually) reduces in magnitude as the Mach number increases, while holding Pr constant. This behaviour is similar to the decline in spanwise and wall-normal Reynolds stresses, seen in Fig. 4, as the Mach number increases and signifies a weakening of the small-scale vortical structures and a movement towards a less active turbulence state. On the other hand, reducing the Prandtl number from 0.7 to 0.2 increases the vorticity fluctuations, affecting all the components. The most likely explanation for this different trend is the reduction in core channel temperature and hence viscosity, meaning that small vortical structures are less damped by viscosity.

3.2. Shocklet structures

As a result of the high values of the mean and turbulent Mach numbers shown in Fig. 3, regions with instantaneous local Mach numbers beyond unity are expected to form in the cases with $M = 0.7$. For such transonic values, the formation of shocklets is possible. Shocklets can be associated with regions where the dilatation, defined as $\theta = \frac{\partial u}{\partial x} + \frac{\partial v}{\partial y} + \frac{\partial w}{\partial z}$, is lower than a negative threshold i.e. $\theta < -\zeta$ (Samtaney et al., 2001; Wang et al., 2017). A value of $\zeta = 3\theta'$, where θ' denotes the dilatation fluctuation (root mean square of the dilatation magnitude) defined as $\theta' = \sqrt{\langle(\frac{\partial u}{\partial x})^2 + (\frac{\partial v}{\partial y})^2 + (\frac{\partial w}{\partial z})^2\rangle}$, has been used in compressible decaying turbulence problems to detect shocklets as regions with strong compression rates (in turbulent Mach number values in the range of $0.5 \leq M_t \leq 1.0$) (Samtaney et al., 2001; Wang et al., 2017). Furthermore, $\zeta = \theta'$ was used by Samtaney et al. (2001) to visualise shocklets. Table 4 provides the bulk-averaged values of the dilatation fluctuation (θ'_b) for the counter-flows studied here as the reference Mach and Prandtl numbers are varied.

In order to detect and visualise the shocklets, iso-surfaces of the dilatation with various threshold values (iso-values) of $\zeta = 2\theta'_b$ (a) and $3\theta'_b$ (b) are used as shown in Fig. 6 for counter-flows with $M \geq 0.4$. The threshold value of $\zeta = 3\theta'_b$ was used by Wang et al. (2017) to highlight the differences in high-compression regions of the flow (i.e. shocklets) as the compressibility increases. The surfaces are coloured based on streamwise velocity (red for positive and blue for negative) to improve their interpretation. We see that significant numbers of shocklet structures are detected. They span the whole computational domain and are highly three-dimensional and irregular. The cases are arranged from top to bottom in order of increasing compressibility, as noted by the increase in θ'_b shown in Table 4. Not only is θ'_b increasing, but also the volume enclosed by shocklet-type structures with dilatation magnitude exceeding $3\theta'_b$ is increasing. The tendency (most clearly in the cases for $M = 0.7$ and $Pr = 0.2$) for the shocklets to be stronger and more frequent at certain spanwise locations in this figure was not generally observed at other time instants, although some connection between shock location and large scale structures cannot be entirely ruled out.

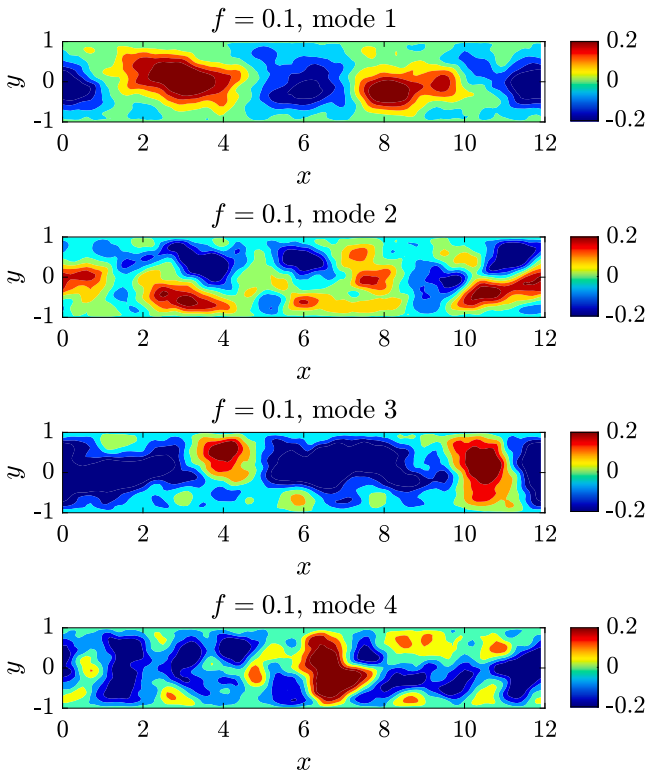

Fig. 11. First 4 SPOD modes on the $x - y$ plane at $f = 0.1$ based on the v component of the velocity vector ($M = 0.7$ and $Pr = 0.7$).

3.3. Shocklet quantification

The total viscous dissipation can be decomposed into the solenoidal and dilatational components as $\epsilon^T = \epsilon^S + \epsilon^D$ (Sarkar et al., 1991) where, the solenoidal (ϵ^S) and dilatational (compressible) (ϵ^D) dissipations are defined as

$$\epsilon^S = \frac{1}{Re}\left[\mu\left\langle\left(\frac{\partial w}{\partial z} - \frac{\partial v}{\partial z}\right)^2 + \left(\frac{\partial u}{\partial z} - \frac{\partial w}{\partial x}\right)^2 + \left(\frac{\partial v}{\partial x} - \frac{\partial u}{\partial y}\right)^2\right\rangle\right] \tag{4}$$

and

$$\epsilon^D = \frac{4}{3Re}\left[\mu\left\langle\frac{\partial u}{\partial x} + \frac{\partial v}{\partial y} + \frac{\partial w}{\partial z}\right\rangle^2\right]. \tag{5}$$

Energy dissipation through Mach number-induced changes on turbulent flow structures (i.e. shocklets) can be linked to the dilatational part of the dissipation (Sarkar et al., 1991). Fig. 7 shows the ratio of the dilatational dissipation to the total dissipation for the counter-flows studied here. The contribution of the dilatational part of the total viscous dissipation becomes significantly more important as the compressibility increases by having a higher Mach number and/or a lower Prandtl number. The peak of the ratio of the dilatational dissipation to the total dissipation occurs at around $|y| \approx 0.75$ for all cases where the mean streamwise velocity and the mean Mach number also exhibit peak values as shown in Fig. 3. It is clear that ϵ^S is directly related to the vorticity which reduces as the Mach number increases. In

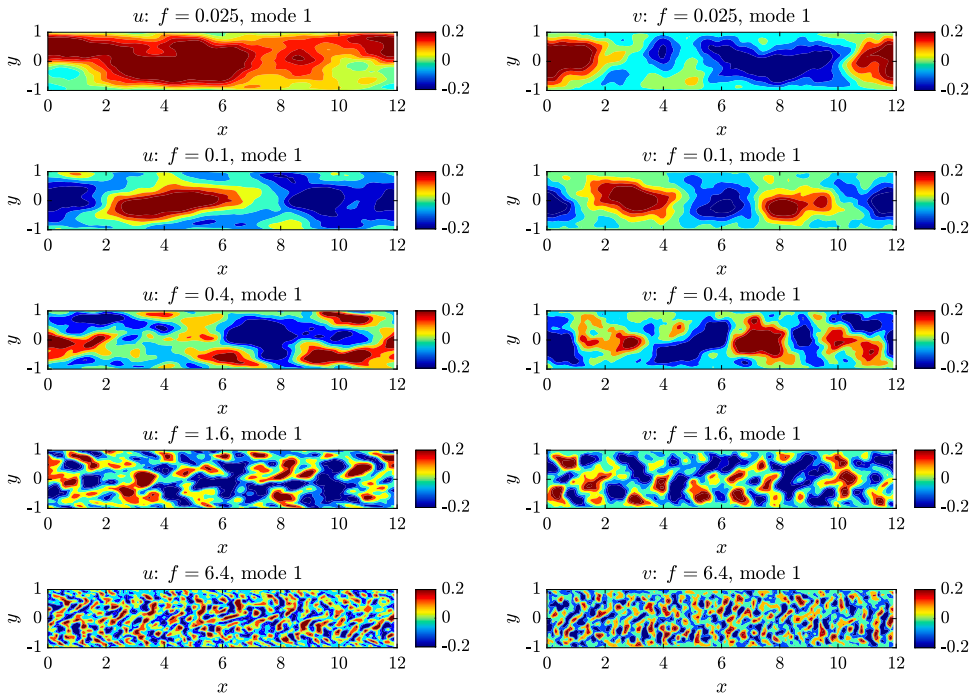

Fig. 12. First SPOD mode on the $x-y$ plane at different frequencies based on the u and v components of the velocity vector ($M = 0.7$ and $Pr = 0.7$).

fact, the solenoidal dissipation reduces slightly (not shown here) as the compressibility of the counter-flow increases. A higher compressibility results in the formation of more shocklets (as shown in Fig. 6), and hence a relatively higher dilatational dissipation.

For a more quantitative analysis of shocklet distribution within the counter-flows, the probability distribution of the dilatation is evaluated, as depicted in Fig. 8. This is based on the Probability Density Function (PDF) of the dilatation, time-averaged over four independent realisations. It presents the PDF of the dilatation across the entire computational domain and on $x-z$ planes at selected channel heights. The PDF profiles for the case with $M = 0.1$ exhibit approximate symmetry, attributable to its low compressibility. As the Mach number increases (or the Prandtl number decreases), the PDF profiles increasingly skew towards negative dilatation values. This skewness stems from the presence of nonlinear compression waves and, ultimately, shocklets within the flow. The trend is consistent at different channel locations indicating that shocklets are present across the entire width of the channel. The only slight difference between the channel centreline (subfigure $y = 0$ plane) and off-centre locations (subfigures $y \approx 0.511$ and 0.962 planes) is that the rate of increase in skewness shows only a small increase from $M = 0.4$ to 0.7, perhaps indicating that the increasing bulk temperature constrains the formation of shocks in this region. When Pr is reduced, hence reducing the bulk temperature, the trend to increasing skewness of the PDF resumes.

To study the variability of shocklets over time, the PDF of the dilatation across the entire domain is plotted for time intervals of $\Delta t = 10$ for the cases with $M = 0.7$ as shown in Fig. 9. The red curves in the graph illustrate the instantaneous PDFs, while the thick black curve signifies their temporal average. It is conspicuous that all the profiles incline towards negative dilatation values, a trend that can be ascribed to the continual presence of shocklets. As previously demonstrated, the counter-flow case with $Pr = 0.2$ exhibits a more negatively skewed profile of the time-averaged dilatation PDF, which aligns with its higher compressibility level.

3.4. SPOD analysis

Fig. 10 shows the energy of spatial SPOD modes as a function of frequency for the analysis based on the u component of the velocity vector on the $x-y$ plane for the case with $M = 0.7$ and $Pr = 0.7$. The SPOD modes and their corresponding mode energies are the eigenvectors and eigenvalues, respectively, of the weighted cross-spectral density matrix, which is estimated from an ensemble of realisations of the temporal discrete Fourier transform (Schmidt, 2022). There is no dominant peak or even distinguishable local peaks in this figure, which confirms the broadband fully turbulent nature of the counter-flow configuration. The integral value of the mode energy over the frequencies (not shown here) decreases monotonically with the mode number. It should be noted that there are similar trends for the mode energies on the $x-z$ plane and also on the $x-y$ plane based on the v component of the velocity vector (not shown here for brevity). There is a rather slow decline in the mode energy as the mode number increases, reflecting the absence of dominant modes compared to the SPOD analysis of flow around a circular cylinder (Chu et al., 2021) or airfoil buffet (Moise et al., 2022), where a global instability is present.

An example of the variability in the SPOD mode shapes is presented in Fig. 11 for the first four modes at a frequency of $f = 0.1$. This figure is based on the v component of the velocity vector on the $x-y$ plane. Mode 1 has its highest amplitude at the centreline $y = 0$ with two spatial wavelengths captured. Higher modes are less coherent and show the presence of peaks closer to the walls. For further study we consider only the first mode.

In Figs. 12 and 13 the first SPOD mode based on the u and v components of the velocity vector is shown on the $x-y$ and $x-z$ planes for different frequencies including $f = 0.025, 0.1, 0.4, 1.6$, and 6.4. On the $x-y$ plane, the lowest two frequencies have modes centred in the middle of the channel where the shear is strongest. At higher frequencies (like $f = 6.4$) the modes include small features that are homogeneously distributed throughout the domain. On the $x-z$ plane the lower frequency modes are in the form of velocity streaks for both the u and v components of the velocity vector. The presence of large-scale streaky structures in the velocity field could potentially be connected the spatial non-uniformity seen in Fig. 6 however inspection of flowfields at other instants in time was not conclusive.

The current analysis did not identify any single dominant large-scale coherent structure in the counter-flow configuration under investigation, which might have been expected for a flow that anticipated to

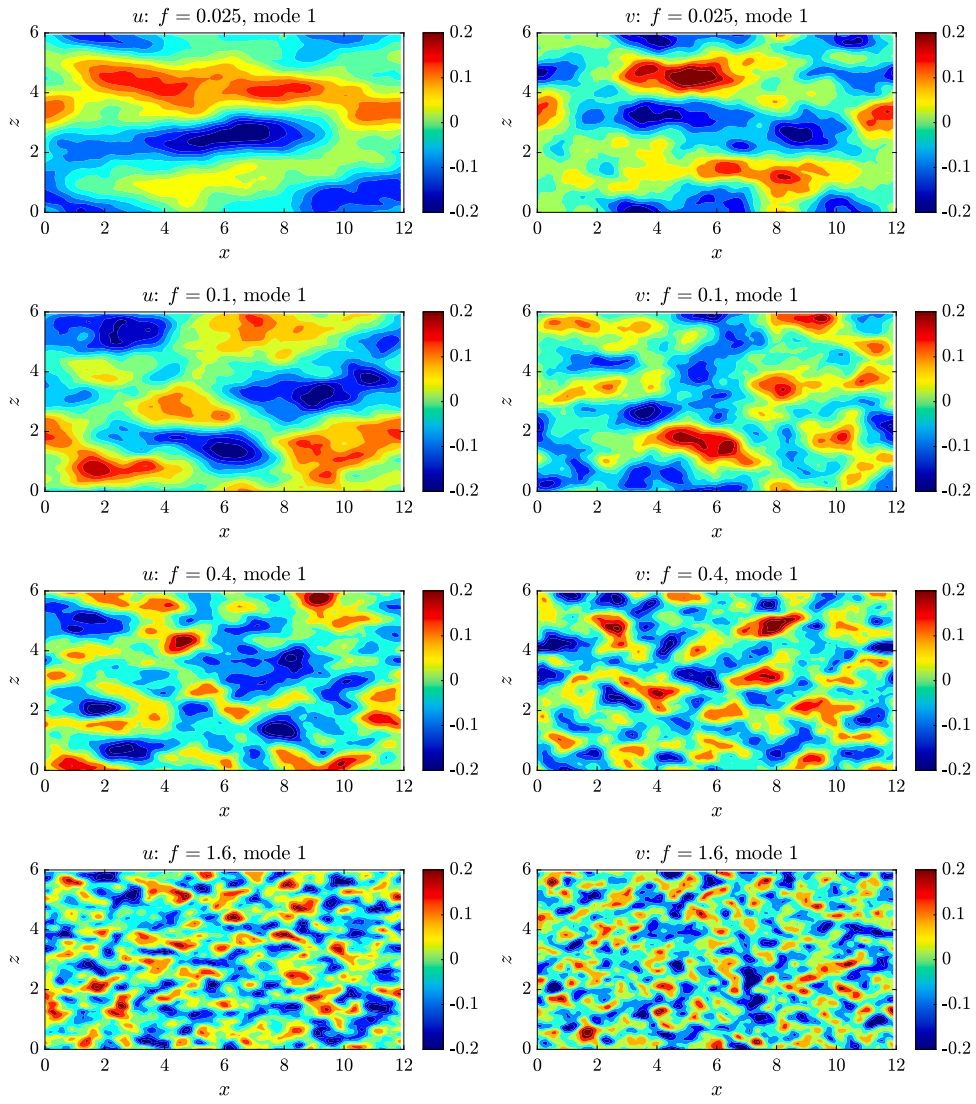

Fig. 13. First SPOD mode on the $x-z$ plane at different frequencies based on the u and v components of the velocity vector ($M = 0.7$ and $Pr = 0.7$).

be globally unstable. Rather, the richness of structures in the SPOD analysis emphasises the broadband three-dimensional nature of the turbulence. The absence of coherent structures does not necessarily eliminate the possibility of underlying associations between the observed streaky structures and oblique modes that are expected to be present in a stability analysis of the mean flow that remains for a future study.

4. Conclusions

Direct numerical simulations of shocklet-containing turbulent flows were conducted using a new counter-flow channel configuration introduced previously by the current authors (Hamzehloo et al., 2021a). The simulations were performed for the reference Mach number values of $M = 0.1, 0.4$ and 0.7 with a Reynolds number of $Re = 400$. A case with a Prandtl number of $Pr = 0.2$ (reduced from the default value of $Pr = 0.7$) and $M = 0.7$ was also studied in an attempt to boost the compressibility within the flow. Additionally, a modal analysis based on SPOD was performed on the $M = 0.7$ and $Pr = 0.7$ counter-flow to better understand the characteristics of the highly three-dimensional transient shocklets embedded in such flow and their interactions with the turbulent scales.

It was found that a reference Mach number as low as $M = 0.7$ could produce fluctuating and mean Mach numbers close to 0.7 over a considerable length of the height of the counter-flow channel. Such values produced instantaneous supersonic velocities that formed relatively strong transient shocklets. Additionally, fluctuating and mean Mach numbers above 0.95 were achieved by reducing the Prandtl number from $Pr = 0.7$ to 0.2 as the core temperature of the flow decreased. Despite the presence of shocklets, the contribution of dilatational dissipation to the total dissipation was found to be small (6% or less) compared to the rotational component. SPOD analysis of the counter flow with $M = 0.7$ and $Pr = 0.7$ showed a small decay of energy with mode number indicating an absence of a single dominant structure. At the lowest frequencies the first SPOD mode appeared in the form of streamwise velocity streaks located at the centre of the channel. While this study did not uncover clear evidence of coherent structures, this does not rule out possible links between the observed streaky structure and the interaction of oblique modes, which a future stability analysis of the mean flow profile may expose.

In summary, the counter-flow configuration of an ideal gas has been shown to be capable of generating highly turbulent flows with embedded compression shocklets for a relatively modest reference

Mach number. Therefore, the configuration provides a useful framework to study some of the fundamental physics associated with shock-turbulence interactions and could be considerably beneficial to the development of compressible sub-grid scale turbulence models as well as improved representations of compressibility in Reynolds-averaged Navier–Stokes models. Future work could include the addition of a heat sink term to the counter-flow configuration, as this would lower the core temperatures and further increase compressibility effects and shocklet generation. Furthermore, the counter-flow could be extended to investigate dense gases, where the molecular complexity can lead to inversion of the fundamental derivative of gas dynamics and a much richer space of permissible non-linear flow structures (Cramer, 1991). Specifically, it would be interesting to demonstrate the existence of expansion shocklets (Giauque et al., 2020) within a dense gas counter-flow, which are not permissible when using an ideal gas equation of state.

Declaration of competing interest

The authors have no conflicts of interest to declare.

Data availability

Data will be made available on request.

Acknowledgements

Dr Arash Hamzehloo was funded by the UK Turbulence Consortium (EPSRC grant EP/R029326/1). Dr David J Lusher was funded by EPSRC grant EP/L015382/1. The authors acknowledge the use of the Cambridge Tier-2 system operated by the University of Cambridge Research Computing Service under an EPSRC Tier-2 capital grant (EP/P020259/1). The flow solver OpenSBLI is available at https://opensbli.github.io.

References

Abdelsamie, A., Janiga, G., Chi, C., Thévenin, D., 2017. Turbulence structure analysis of DNS data using DMD and SPOD: mixing jet and channel flow. In: Progress in Turbulence VII: Proceedings of the ITi Conference in Turbulence 2016. Springer, pp. 199–204.

Abreu, L.I., Cavalieri, A.V., Schlatter, P., Vinuesa, R., Henningson, D.S., 2020. Resolvent modelling of near-wall coherent structures in turbulent channel flow. Int. J. Heat Fluid Flow 85, 108662.

Alvi, F., Strykowski, P., 1999. Forward flight effects on counterflow thrust vector control of a supersonic jet. AIAA J. 37 (2), 279–281.

Brehm, C., Barad, M.F., Housman, J.A., Kiris, C.C., 2015. A comparison of higher-order finite-difference shock capturing schemes. Comput. & Fluids 122, 184–208.

Carpenter, M.H., Nordström, J., Gottlieb, D., 1999. A stable and conservative interface treatment of arbitrary spatial accuracy. J. Comput. Phys. 148 (2), 341–365.

Chu, S., Xia, C., Wang, H., Fan, Y., Yang, Z., 2021. Three-dimensional spectral proper orthogonal decomposition analyses of the turbulent flow around a seal-vibrissa-shaped cylinder. Phys. Fluids 33 (2), 025106.

Coleman, G., Kim, J., Moser, R., 1995. A numerical study of turbulent supersonic isothermal-wall channel flow. J. Fluid Mech. 305, 159–183.

Cramer, M., 1991. Nonclassical dynamics of classical gases. Nonlinear Waves Real Fluids 91–145.

Ducros, F., Laporte, F., Soulères, T., Guinot, V., Moinat, P., Caruelle, B., 2000. High-order fluxes for conservative skew-symmetric-like schemes in structured meshes: application to compressible flows. J. Comput. Phys. 161 (1), 114–139.

Feiereisen, W.J., 1981. Numerical simulation of a compressible homogeneous, turbulent shear flow (Ph.D. thesis). Stanford Univ., CA., Stanford Univ., CA., Stanford Univ., CA.

Forliti, D., Tang, B., Strykowski, P., 2005. An experimental investigation of planar countercurrent turbulent shear layers. J. Fluid Mech. 530, 241.

Freund, J., Lele, S., Moin, P., 2000. Compressibility effects in a turbulent annular mixing layer. Part 1. Turbulence and growth rate. J. Fluid Mech. 421, 229–267.

Giauque, A., Corre, C., Vadrot, A., 2020. Direct numerical simulations of forced homogeneous isotropic turbulence in a dense gas. J. Turbul. 21 (3), 186–208.

Gillgrist, R., Forliti, D., Strykowski, P.J., 2007. On the mechanisms affecting fluidic vectoring using suction. J. Fluids Eng. 129 (1).

Hamzehloo, A., Lusher, D., Laizet, S., Sandham, N., 2021a. Direct numerical simulation of compressible turbulence in a counter-flow channel configuration. Phys. Rev. Fluids 6 (9), 094603.

Hamzehloo, A., Lusher, D.J., Laizet, S., Sandham, N.D., 2021b. On the performance of WENO/TENO schemes to resolve turbulence in DNS/LES of high-speed compressible flows. Internat. J. Numer. Methods Fluids 93 (1), 176–196.

Humphrey, J., Li, S., 1981. Tilting, stretching, pairing and collapse of vortex structures in confined counter-current flow. J. Fluids Eng. 103 (3).

Jiang, G.-S., Shu, C.-W., 1996. Efficient implementation of weighted ENO schemes. J. Comput. Phys. 126 (1), 202–228.

Johnstone, R., Coleman, G.N., Spalart, P.R., 2010. The resilience of the logarithmic law to pressure gradients: evidence from direct numerical simulation. J. Fluid Mech. 643, 163–175.

Kim, J., Moin, P., Moser, R., 1987. Turbulence statistics in fully developed channel flow at low Reynolds number. J. Fluid Mech. 177, 133–166.

Lee, S., Lele, S.K., Moin, P., 1991. Eddy shocklets in decaying compressible turbulence. Phys. Fluids A 3 (4), 657–664.

Lele, S.K., 1994. Compressibility effects on turbulence. Annu. Rev. Fluid Mech. 26 (1), 211–254.

Li, Q., 2003. Numerical study of Mach number effects in compressible wall-bounded turbulence (Ph.D. thesis). University of Southampton.

Lonnes, S., Hofeldt, D., Strykowski, P., 1998. Flame speed control using a countercurrent swirl combustor. In: 36th AIAA Aerospace Sciences Meeting and Exhibit. p. 352.

Lusher, D.J., Coleman, G.N., 2022. Numerical study of compressible wall-bounded turbulence – the effect of thermal wall conditions on the turbulent Prandtl number in the low-supersonic regime. Int. J. Comput. Fluid Dyn. 36 (9), 797–815.

Lusher, D., Jammy, S., Sandham, N., 2021. OpenSBLI: Automated code-generation for heterogeneous computing architectures applied to compressible fluid dynamics on structured grids. Comput. Phys. Comm. 108063.

Lusher, D.J., Sandham, N., 2019. Assessment of low-dissipative shock-capturing schemes for transitional and turbulent shock interactions. In: AIAA Aviation 2019 Forum. p. 3208.

Lusher, D.J., Zauner, M., Sansica, A., Hashimoto, A., 2023. Automatic code-generation to enable high-fidelity simulations of multi-block airfoils on GPUs. In: AIAA SCITECH 2023 Forum. AIAA 2023–1222.

Mankbadi, M.R., DeBonis, J.R., Georgiadis, N.J., 2017. Large-eddy simulation of a compressible mixing layer and the significance of inflow turbulence. In: 55th AIAA Aerospace Sciences Meeting. p. 0316.

Modesti, D., Pirozzoli, S., 2016. Reynolds and Mach number effects in compressible turbulent channel flow. Int. J. Heat Fluid Flow 59, 33–49.

Moise, P., Zauner, M., Sandham, N.D., 2022. Large-eddy simulations and modal reconstruction of laminar transonic buffet. J. Fluid Mech. 944, A16.

Mudalige, G., Reguly, I., Jammy, S., Jacobs, C., Giles, M., Sandham, N., 2019. Large-scale performance of a DSL-based multi-block structured-mesh application for direct numerical simulation. J. Parallel Distrib. Comput. 131, 130–146.

Muralidhar, S.D., Podvin, B., Mathelin, L., Fraigneau, Y., 2019. Spatio-temporal proper orthogonal decomposition of turbulent channel flow. J. Fluid Mech. 864, 614–639.

Pirozzoli, S., 2011. Numerical methods for high-speed flows. Annu. Rev. Fluid Mech. 43 (1), 163–194.

Reguly, I.Z., Mudalige, G.R., Giles, M.B., Curran, D., McIntosh-Smith, S., 2014. The OPS domain specific abstraction for multi-block structured grid computations. In: Fourth International Workshop on Domain-Specific Languages and High-Level Frameworks for High Performance Computing. IEEE, pp. 58–67.

Samtaney, R., Pullin, D., Kosović, B., 2001. Direct numerical simulation of decaying compressible turbulence and shocklet statistics. Phys. Fluids 13 (5), 1415–1430.

Sarkar, S., 1995. The stabilizing effect of compressibility in turbulent shear flow. J. Fluid Mech. 282, 163–186.

Sarkar, S., Erlebacher, G., Hussaini, M., Kreiss, H., 1991. The analysis and modelling of dilatational terms in compressible turbulence. J. Fluid Mech. 227, 473–493.

Schmidt, O.T., 2022. Spectral proper orthogonal decomposition using multitaper estimates. Theor. Comput. Fluid Dyn. 36 (5), 741–754.

Schmidt, O.T., Towne, A., 2019. An efficient streaming algorithm for spectral proper orthogonal decomposition. Comput. Phys. Comm. 237, 98–109.

Shu, C.-W., 1997. Essentially non-oscillatory and weighted essentially non-oscillatory schemes for hyperbolic conservation laws. ICASE Rep. (97–65), 1–78.

Strykowski, P.J., Krothapalli, A., Forliti, D., 1996. Counterflow thrust vectoring of supersonic jets. AIAA J. 34 (11), 2306–2314.

Strykowski, P., Wilcoxon, R., 1993. Mixing enhancement due to global oscillations in jets with annular counterflow. AIAA J. 31 (3), 564–570.

Terakado, D., Nonomura, T., Kawai, S., Aono, H., Sato, M., Oyama, A., Fujii, K., 2022. Sound source characteristics generated by shocklets in isotropic compressible turbulence. Phys. Rev. Fluids 7, 084605.

Towne, A., Schmidt, O.T., Colonius, T., 2018. Spectral proper orthogonal decomposition and its relationship to dynamic mode decomposition and resolvent analysis. J. Fluid Mech. 847, 821–867.

Vreman, A., Sandham, N., Luo, K., 1996. Compressible mixing layer growth rate and turbulence characteristics. J. Fluid Mech. 320, 235–258.

Waleffe, F., 1990. On the three-dimensional instability of strained vortices. Phys. Fluids A 2 (1), 76–80.

Wang, J., Gotoh, T., Watanabe, T., 2017. Shocklet statistics in compressible isotropic turbulence. Phys. Rev. Fluids 2 (2), 023401.

Williamson, J., 1980. Low-storage Runge-Kutta schemes. J. Comput. Phys. 35 (1), 48–56.

Yao, J., Hussain, F., 2020. Turbulence statistics and coherent structures in compressible channel flow. Phys. Rev. Fluids 5 (8), 084603.

Yee, H., Sjögreen, B., 2018. Recent developments in accuracy and stability improvement of nonlinear filter methods for DNS and LES of compressible flows. Comput. & Fluids 169, 331–348.